Earth and Planetary Science Letters 500 (2018) 97–104

Contents lists available at ScienceDirect

Earth and Planetary Science Letters

www.elsevier.com/locate/epsl

Fragmentation and Plinian eruption of crystallizing basaltic magma

Pranabendu Moitra [a,b,*], Helge M. Gonnermann [b], Bruce F. Houghton [c], Chandra S. Tiwary [d,e]

[a] Department of Geology and Center for Geohazards Studies, University at Buffalo, Buffalo, NY, USA
[b] Department of Earth, Environmental and Planetary Sciences, Rice University, TX, USA
[c] Department of Geology and Geophysics, University of Hawai'i at Manoa, Honolulu, USA
[d] Department of Material Science and NanoEngineering, Rice University, Houston, TX, USA
[e] Materials Science and Engineering, Indian Institute of Technology Gandhinagar, Gujarat, India

ARTICLE INFO

Article history:
Received 14 December 2017
Received in revised form 30 July 2018
Accepted 2 August 2018
Available online xxxx
Editor: T.A. Mather

Keywords:
basaltic Plinian eruption
explosive magma fragmentation
oscillatory shear rheometry
extensional rheometry
bubble growth and crystallization
conduit model

ABSTRACT

Basalt is the most ubiquitous magma on Earth, erupting typically at intensities ranging from quiescently effusive to mildly explosive. The discovery of highly explosive Plinian eruptions of basaltic magma has therefore spurred debate about their cause. Silicic eruptions of similar style are a consequence of brittle fragmentation, as magma deformation becomes progressively more viscoelastic. Magma eventually crosses the glass transition and fragments due to a positive feedback between water exsolution, viscosity and decompression rate. In contrast to silicic eruptions, the viscosity of basaltic magmas is thought to be too low to reach conditions for brittle fragmentation. Pyroclasts from several basaltic Plinian eruptions, however, contain abundant micron-size crystals that can increase magma viscosity substantially. We therefore hypothesize that magma crystallization led to brittle fragmentation during these eruptions. Using combined oscillatory and extensional rheometry of concentrated particle-liquid suspensions that are dynamically similar to microcrystalline basaltic magma, we show that high volume fractions of particles and extension rates of about 1 s^{-1} or greater result in viscoelastic deformation and brittle fracture. We further show that for experimentally observed crystallization rate, basaltic magma can reach the empirical failure conditions when erupting at high discharge rates.

1. Introduction

The fragmentation and dynamics of Plinian eruptions of basaltic magma have been a subject of debate (e.g., Giordano and Dingwell, 2003; Houghton and Gonnermann, 2008; Costantini et al., 2010; Goepfert and Gardner, 2010). The critical deformation rate at which silicate melt dynamically crosses the glass transition is $\sim 10^{-2}/\tau_{relax}$ (e.g., Dingwell and Webb, 1989). Here τ_{relax} is the relaxation time scale of silicate melts, defined as $\tau_{relax} = \eta_0/G_\infty$, where η_0 is the shear viscosity at zero frequency, and $G_\infty \sim 10$ GPa is the shear modulus at infinite frequency. For crystal-poor basaltic melt η_0 is of the order of 10^2–10^3 Pa s (Hui and Zhang, 2007) and τ_{relax} is 10^{-8}–10^{-7} s. Deformation rates of greater than 10^5 s^{-1} would be required for basaltic melt to reach the glass transition, which is difficult to reconcile with the dynamics of magma ascent (e.g., Wilson and Head, 1981; Papale, 1999). Consequently, fragmentation during explosive basaltic eruptions is thought to be of hydrodynamic nature (e.g., Parfitt, 2004; Namiki and Manga, 2008; Valentine and Gregg, 2008; Gonnermann, 2015).

Pyroclastic eruptive deposits from several explosive basaltic eruptions, for example the 1886 eruption of Mt. Tarawera (Sable et al., 2009), New Zealand and the 122 BCE eruption of Mt. Etna, Italy (Coltelli et al., 1998; Sable et al., 2006), indicate sustained eruption columns of approximately 25–30 km height, over durations of hours, and at mass discharge rates of about 10^8 kg s^{-1}. They are therefore classified as Plinian eruptions. Recent quantitative studies on these eruptions used existing stress- or strain rate-driven fragmentation criteria (e.g., Moitra et al., 2013; Campagnola et al., 2016). However due to very small τ_{relax}, as discussed above, the question remains whether in analogy to their silicic counterparts these eruptions were associated with brittle fragmentation. The pyroclasts from these eruptions contain a high abundance of micron-size crystals (up to 90% in volume of the matrix; Fig. 1) that likely formed as a consequence of water exsolution during eruptive magma ascent (e.g., Hammer and Rutherford, 2002; Goepfert and Gardner, 2010; Arzilli et al., 2015).

To assess whether microlites affect the mechanics of magma fragmentation, this study uses a novel approach by examining

* Corresponding author at: Department of Geology and Center for Geohazards Studies, University at Buffalo, Buffalo, NY, USA.
E-mail address: pranaben@buffalo.edu (P. Moitra).

https://doi.org/10.1016/j.epsl.2018.08.003
0012-821X/

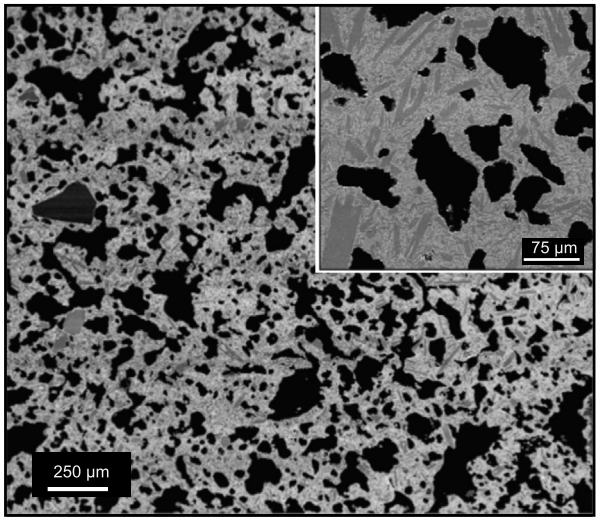

Fig. 1. Back-scattered electron (BSE) images of pyroclast sections from Mt. Tarawera, 1886 basaltic Plinian eruption. The inset shows two distinct microlite populations with larger high aspect ratio plagioclase crystals and smaller equigranular to high aspect ratio plagioclase and pyroxene crystals in the glass matrix (gray) surrounding vesicles (black).

the extensional deformation and fracture behavior of concentrated liquid-particle suspensions that are dynamically similar to microcrystalline basaltic magma. Using scaling analysis and conduit model of magma ascent in volcanic conduit, it is demonstrated that under what conditions crystallizing basaltic magma can reach brittle fragmentation during explosive Plinian style eruptive activity.

2. Experimental methods

2.1. Overview

We performed a series of experiments in viscous fluids with suspended micron-size solid particles to assess the potential effect of high microlite concentrations on the rheological behavior of basaltic magmas. These suspensions have rheological properties that are dynamically similar to basaltic melt with high volume fraction of microlites (see Appendix A). The suspensions consisted of silicone oil with a Newtonian shear viscosity of 100 Pa s and 3–10 μm glass spheres at a volume fraction of $\phi_x = 0.55$, which is close to the maximum packing limit of $\phi_m = 0.56$. To characterize the viscoelastic properties of the concentrated suspension and its potential for fracture development, we performed oscillatory shear and extensional deformation experiments (Fig. 2). Particle settling was negligible during our experiments because the characteristic settling time was much smaller than the experimental time scales.

2.2. Oscillatory shear rheology

Oscillatory shear experiments, consisting of amplitude and frequency sweeps (e.g., Heymann et al., 2002; Sumita and Manga, 2008; Namiki and Tanaka, 2017), were performed using an Anton Paar Physica MCR 301^{TM} rotational rheometer with parallel plate geometry and a 1 mm gap (Fig. 2a). The amplitude sweep experiments were performed at a fixed angular frequency, ω, in the range of 10^{-1} to 10^{2} rad s^{-1} and 10^{-4} to 10^{-1} of total strain, γ_s. The frequency sweep experiments were performed at angular frequency of 10^{-1} to 10^{2} rad s^{-1} and a fixed strain amplitude of about 10^{-4}, which corresponds to the linear viscoelastic range obtained from the amplitude sweep experiments. In order to

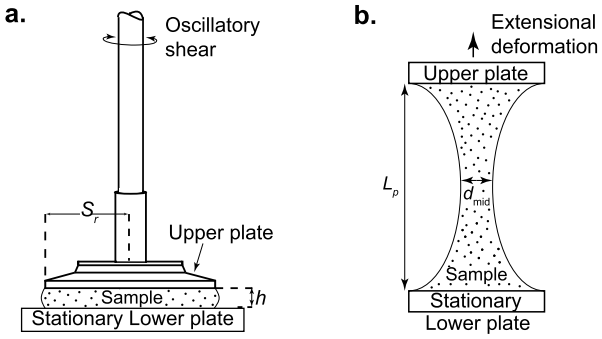

Fig. 2. Schematic diagrams of experimental methods. (**a**) The oscillatory shear rheology experiments were performed using a parallel-plate geometry, where S_r is the radius of the disk of sample in between two plates, and h is the sample thickness. (**b**) The extensional rheometry (tensile test) was performed by placing a cylindrical sample in between two parallel plates, where the upper plate moved upward while the lower plate stayed stationary. L_p is the plate separation length and d_{mid} is the diameter at the middle of the cylindrical sample.

avoid normal forces due to sample placement, the samples were pre-sheared. The resultant complex shear modulus, G^*, can be expressed as

$$G^* = G' + iG'', \tag{1}$$

where G' and G'' are the storage or elastic shear modulus and the loss or viscous shear modulus, respectively.

2.3. Extensional rheometry

The extensional rheometry (tensile tests) was performed using an Instron Electropuls^{TM} E3000. The suspension was placed between two parallel plates that moved apart in the vertical direction, resulting in an increase in the gap between the two plates (Fig. 2b). In order to obtain a purely uniaxial elongation the gap was increased at an exponentially increasing rate (e.g., McKinley and Sridhar, 2002; White et al., 2010). The position of the upper moving plate is thus given as

$$L_p(t) = L_0 \exp(\dot{E}t), \tag{2}$$

where L_0 is the initial gap length (i.e., the initial length of the sample), t is time, and $\dot{E} = \dot{L_p}/L_p$ is the axial stretch rate. Equivalent to pre-shearing in shear rheology experiments, a small initial stretch rate of ≈0.05 s^{-1} was applied for few seconds prior to each experiment.

The elongating fluid in the center of the gap underwent a nearly shear-free flow whose effective extensional rate of deformation can be defined as

$$\dot{\gamma}_{\text{eff}}(t) = \frac{-2}{d_{\text{mid}}} \frac{d(d_{\text{mid}})}{dt}, \tag{3}$$

where d_{mid} is the diameter at the middle of the suspension filament. The effective Hencky strain is defined as

$$\gamma_{\text{eff}} = 2 \ln \left(\frac{d_0}{d_{\text{mid}}} \right), \tag{4}$$

where d_0 is the initial diameter of the sample at its midpoint and is much greater than the particle diameter. The change in mid-filament radius with respect to time was calculated from conservation of fluid volume and with the aid of photographs of the extending cylindrical sample.

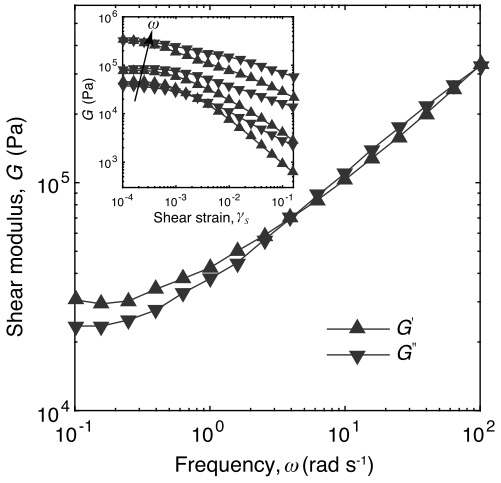

Fig. 3. Results of oscillatory shear rheology. The storage and loss shear moduli, G' and G'', respectively, as functions of the angular frequency, ω. The inset shows the amplitude sweep tests during which the linear viscoelastic region ($G' \geq G''$) was observed at lower strain, γ_s, for $10^{-1} < \omega < 10^{2}$ rad s^{-1}. Multiple crossovers between G' and G'' in frequency sweep test are often observed in viscoelastic dense particulate suspensions (e.g., Sumita and Manga, 2008).

3. Results and discussion

3.1. Experimental results

Fig. 3 indicates that under oscillatory shear deformation the dense particulate suspension behaves like a viscoelastic material, with a crossover between the storage (elastic) modulus, G', and the loss (viscous) modulus, G'' (Fig. 3). The viscoelastic rheological response is attributable to particle interactions and jamming at volume fractions close to maximum packing. The uniaxial extensional experiments show that the sample undergoes brittle fracture at elongation rates greater than about 1 s^{-1}. In contrast, the suspending liquid without suspended particles does not fracture (Fig. 4). Consistent with the oscillatory experiments, we interpret fracturing to be a consequence of viscoelastic behavior at high deformation rates.

3.2. Potential implications for basaltic Plinian eruptions

We hypothesize that a viscoelastic rheological response, due to magma expansion, may also be possible during volcanic eruption of micro-crystalline basaltic magmas. We propose that this requires crystal volume fractions close to maximum packing, as well as magma elongation at rates above some threshold value, $\dot{\gamma}_{cr}$. In the absence of elongation experiments on highly microcrystalline basaltic melt, we assume dynamic similarity of our experiments and a failure condition of $\dot{\gamma}_{cr} > \sim 1$ s^{-1}.

Conceptually, we envisage that the basaltic magma crystallizes during eruptive ascend (e.g., Cashman, 1993; Hammer and Rutherford, 2002; Goepfert and Gardner, 2010; Applegarth et al., 2013; Shea and Hammer, 2013; Arzilli et al., 2015). As pressure decreases with height within the volcanic conduit, the ascending magma vesiculates due to decrease in the solubility of dissolved volatiles. The resultant volume expansion and acceleration are a consequence of bubble growth, which stretches the surrounding crystallizing melt. If the vesiculating magma can reach sufficiently high crystallinity and expansion rates, we hypothesize that it may fracture in a similar fashion as the suspension in our elongation experiments. Assuming that the critical elongation rate for brittle failure in our experiments provides a reasonable failure criterion for microcrystalline basaltic magma, the question is whether and under which conditions a crystal volume fraction of ϕ_x/ϕ_m close to 1, together with the failure criterion $\dot{\gamma}_{cr}$ can be reached during eruptions. We explore these considerations subsequently.

3.2.1. Crystallization

Crystallization involves both crystal nucleation and growth. The Avrami equation provides a well-known quantification of crystallization kinetics, and is given by (e.g., Cashman, 1993)

$$\phi_x = 1 - \exp\left(-k_v I F^3 t^4\right). \tag{5}$$

Here ϕ_x is the crystal volume fraction, k_v is the shape factor, I is the crystal nucleation rate, F is the crystal growth rate, and t is time. Given I and F, the Avrami equation facilitates the calculation of crystal volume fraction, ϕ_x, as a function of time. Fig. 5a shows existing experimental values for I and F in silicate melts

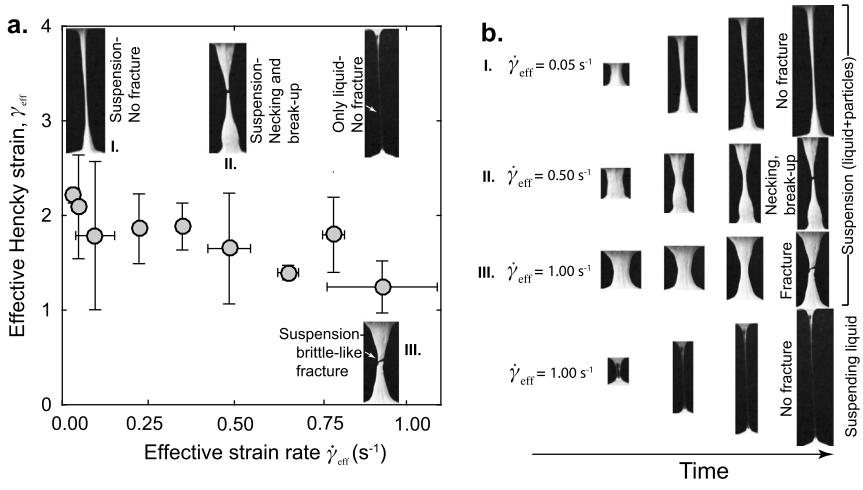

Fig. 4. Results of uniaxial extension experiments. (**a**) With increasing elongation rates, the suspension progresses from (I.) simple elongation to (II.) ductile necking and break-up to (III.) brittle fracturing, as shown by the experimental images (white arrow indicates irregular and angular fracturing at higher strain rate). In comparison, the existence of a thin liquid film of the suspending liquid is observed (also indicated by white arrow in the top, right image) at higher strain rates. The error bars indicate the reproducibility of experiments and the error associated with the measurement of sample mid-radius using the experimental images. (**b**) The experimental image sequences show the progressive extension of the particulate suspension filament with time at various extensional strain rates, as well as the extension of the particle-free suspending liquid (bottom row) at a higher strain rate for comparison. The initial mid-radii at the onset of experiments were 4 mm, 6 mm and 5 mm for cases I, II and III, respectively. The corresponding final mid-radii were 1 mm, 0.5 mm and 2.0 mm. The initial and final mid-radii of the thin filament of particle-free liquid were about 1.5 mm and 0.15 mm, respectively.

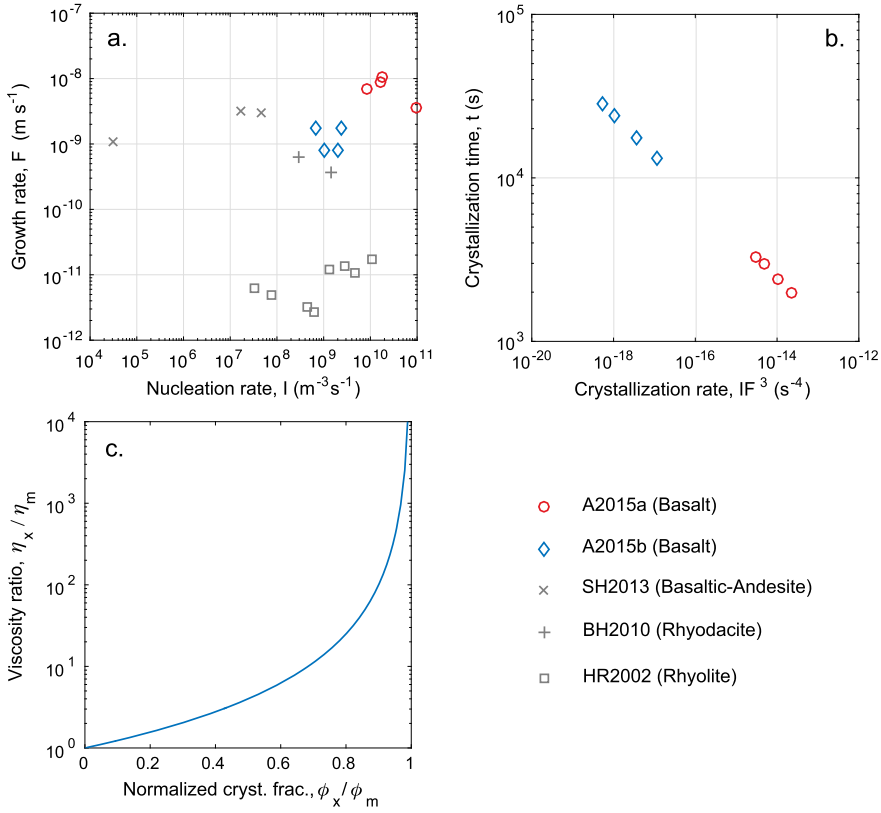

Fig. 5. (**a**) Values of the crystal growth rate, F, and the crystal nucleation rate, I, from decompression–crystallization experiments. The data shown are from the recent compilation by Arzilli et al. (2015), where A2015a and A2015b are from Arzilli et al. (2015), HR2002 is from Hammer and Rutherford (2002), BH2010 is from Brugger and Hammer (2010) and SH2013 is from Shea and Hammer (2013). (**b**) Calculation of the time required for basaltic melts to reach high crystallinity (i.e., $\phi_x \rightarrow \phi_m$), using the Avrami equation (equation (5)). The size of the symbols span time scales corresponding to $0.60 \leq \phi_m \leq 0.90$, the observed range of microlites in the pyroclasts from basaltic Plinian eruptions at Mt. Etna and Mt. Tarawera. (**c**) The change in magma (melt+crystal) viscosity, η_x, to the melt viscosity, η_m, as a function of normalized crystal volume fraction, ϕ_x/ϕ_m. η_x increases in a highly nonlinear fashion as $\phi_x \rightarrow \phi_m$.

from the compilation of Arzilli et al. (2015). When used in conjunction with the Avrami equation these data provide constraints on the time required for basaltic melt to crystallize to values of ϕ_x close to ϕ_m, where the latter may depend on crystal shape and size distribution (e.g., Moitra and Gonnermann, 2015). Here we assume that $k_v = 4\pi/3$ for spherical crystals, and $\phi_m = 0.60$–0.90, noting that the specific value does not affect our estimates significantly. Based on the experimentally determined values of I and F, Fig. 5b shows that basaltic magma can reach crystal volume fractions close to maximum packing in about 10^3 s. For storage depths corresponding to a few kilometers this implies that basaltic magma can extensively crystallize, if it ascends at velocities of several meters per second. In the case of the 1886 eruption of Mt. Tarawera, for example, such velocities are consistent with discharge rate estimates of about 10^5 m^3 s^{-1} (Sable et al., 2009), given that the eruption appears to have been fed from an approximately 17 km-long dike and assuming a dike-width of up to a few meters.

3.2.2. Viscosity

In a general sense the viscosity of the liquid-particle suspension, η_x, increases with increasing ϕ_x. This relation can be defined as (e.g., Mader et al., 2013; Moitra and Gonnermann, 2015)

$$\eta_x = \eta_m \left(1 - \frac{\phi_x}{\phi_m}\right)^{-2}, \tag{6}$$

where η_m is the viscosity of the pure melt. As $\phi_x \rightarrow \phi_m$ the value of η_x increases in a highly nonlinear fashion (Fig. 5c). We will show that this increase in viscosity, assuming that the eruption is sustained and has adjusted to magma crystallization, leads to a proportional increase in decompression rate, and that this dependency or feedback can potentially drive conditions toward brittle failure.

3.2.3. Decompression rate

To assess under which conditions brittle failure can occur during basaltic eruptions, we first consider the relation between decompression rate and magma crystallization. In general the decompression rate of erupting magma encompasses magma-static and viscous stresses. If the magma is to undergo brittle fragmentation, as the volume fraction of crystals approaches the maximum packing fraction, then the value of $\dot{\gamma}_{cr}$ provides a conditional constraint on decompression rate.

The momentum balance for a growing bubble, neglecting surface tension and inertial terms, provides an expression for the elongation rate, $\dot{\gamma}_E$ (e.g., Proussevitch et al., 1993)

$$\dot{\gamma}_E = \frac{1}{R}\frac{dR}{dt} = \frac{1}{\eta_x}\left(P_g - P_m\right). \tag{7}$$

Here R is the bubble radius, η_x is the viscosity of the crystalline melt, P_g is pressure of the gas inside bubbles, P_m is the pressure of the surrounding crystalline melt, and t is time. Equation (7) indicates that for $\dot{\gamma}_E$ to attain its critical value, for a given value of η_x at $\phi_x/\phi_m \rightarrow 1$, requires that $(P_g - P_m)$ also reaches some critical value. This in turn implies that the rate of decrease in melt pressure is larger than the rate of decrease in gas pressure within bubbles, such that

$$\left|\frac{dP_m}{dt}\right| > \left|\frac{dP_g}{dt}\right|. \tag{8}$$

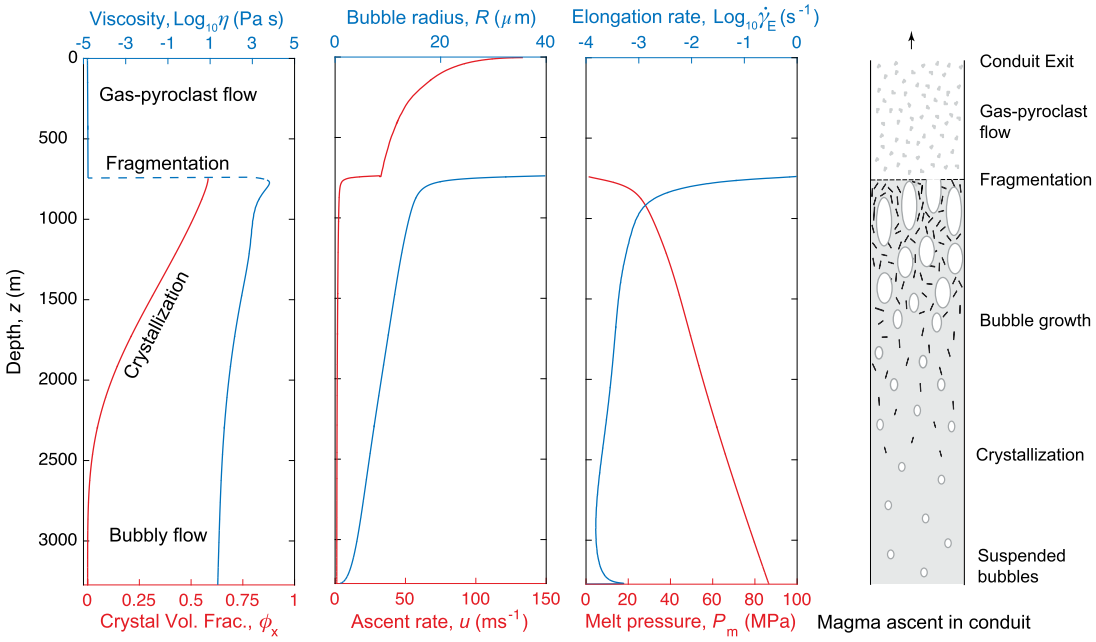

Fig. 6. Illustrative example of how variables evolve during basaltic magma ascent in a dike-like conduit (see Appendix B for details). The calculation corresponds to a dike width and length of $2a = 1.2$ m and $b = 5$ km, respectively. Other conditions are: crystallization rate of $IF^3 = 10^{-13.5}$ s^{-4}, bubble number density of $N_b = 10^{14}$ m^{-3}, maximum crystal packing fraction of $\phi_m = 0.60$, initial dissolved H_2O of $c_o = 3$ wt%, magma temperature of $T = 1100°C$, and the initial bubble radius of $R_o = 10^{-6}$ m. It is assumed that the magma fragments at the empirically obtained critical strain rate of $\dot{\gamma}_{cr} = 1.0$ s^{-1}. Furthermore, it is assumed that there are no bubble and crystal growth after fragmentation, therefore their values are only shown up to fragmentation, along with the value of melt pressure. The model illustrates the interdependencies between crystallization, bubble and crystal bearing multiphase magma viscosity, pressure decrease, and elongation rate. (For interpretation of the references to color in this figure, the reader is referred to the web version of this article.)

From the mass balance of a growing bubble (e.g., Proussevitch et al., 1993), the right hand term in Equation (8) is given by

$$\frac{dP_g}{dt} = -\frac{3P_g}{R}\frac{dR}{dt} = -3P_g\dot{\gamma}_E. \tag{9}$$

Thus, for a critical failure criterion of $\dot{\gamma}_E = \dot{\gamma}_{cr}$,

$$\left|\frac{dP_m}{dt}\right| > P_g\dot{\gamma}_{cr}. \tag{10}$$

Basaltic Plinian pyroclasts, for example from Mt. Etna and Mt. Tarawera eruptions have vesicularities of ≈50–80% (Sable et al., 2006, 2009). If they represent magmatic conditions near fragmentation, solubility and equation of state indicate gas pressures of about 1–10 MPa. Such values of P_g and $\dot{\gamma}_{cr} = 1$ s^{-1} give a conditional failure constraint for decompression rates of

$$\left|\frac{dP_m}{dt}\right| > 1\,\text{MPa}\,\text{s}^{-1}. \tag{11}$$

An order of magnitude estimate of corresponding eruption rates can be obtained from the momentum balance of the erupting magma. Assuming basaltic melt viscosity of $10^2 - 10^3$ Pa s, as $\phi_x \to \phi_m$ the viscosity of the crystallizing magma will be $\eta_x \sim 10^6 - 10^7$ Pa s (Fig. 5c). At velocities of several meters per second, and to first order neglecting any shear-rate dependence of viscosity during flow within the conduit, decompression rates are predominantly due to viscous stresses associated with laminar magma flow. Assuming that magma is ascending within a dike-like conduit of width $2a$, as appears to have been the case for Mt. Tarawera in 1886, an estimate for decompression rate can be obtained from the force balance of steady flow between parallel plates (Bird et al., 2002)

$$\left|\frac{dP_m}{dt}\right| = \frac{3\eta_x u^2}{4a^2} \gtrapprox 1\,\text{MPa}\,\text{s}^{-1}, \tag{12}$$

where $u^2/4a^2 \approx 1$ s^{-2}. This value is within range of the conditional constraint obtained from momentum balance of growing bubble (Equation (11)). We therefore suggest that it may be feasible to attain conditions for brittle failure for basaltic Plinian eruptions.

3.3. Illustrative model

Within the framework of our hypothesis, requirements for brittle failure of basaltic magma are (1) elongation rates of $\dot{\gamma}_E = \dot{\gamma}_{cr} \sim 1$ s^{-1}; (2) microcrystallinity at volume fractions, ϕ_x, near the maximum packing fraction; and (3) decompression rates of about 1 MPa s^{-1} or greater. In the previous sections we provided a scaling analysis to demonstrate that these failure conditions might be reached during the Plinian eruption of basaltic magma. A key consideration is that these conditions can only be achieved as the volume fraction of microlites reaches values that are close to their maximum packing fraction. This would be the case after the magma has risen over a significant distance from the chamber, assuming that crystallization is occurring during ascent. The strongly nonlinear effect of crystals on viscosity is also expected to drive the erupting magma towards decompression rates that are increasing proportionally to the viscosity. Once the estimated decompression rate required for fragmentation is reached, we expect the aforementioned nonlinearities to drive the system toward fragmentation within seconds.

This is illustrated in Fig. 6, which provides an example calculation of basaltic magma ascent through a dike, and at discharge rates similar to the 1886 basaltic Plinian eruption of Mt. Tarawera. The calculations that produced this illustrative example are based on mass and momentum balance equations for magma and magmatic volatiles, together with crystallization based on the Avrami equation and shear-rate dependent magma viscosity that accounts for the presence of crystals and bubbles (see Appendix B for details). The model assumes that the eruption is sustained at approximately steady discharge rates for a duration that is longer than the magma ascent and crystallization time. In other words, the erup-

tion has adjusted to crystallization. It can be seen that viscosity increases by more than an order of magnitude over a distance of a few 100 meters, even though ϕ_x only increases by a small fraction as $\phi_x \rightarrow \phi_m$. As a consequence, pressure decreases by tens of MPa over the same distance. This leads to a rapid increase in the rate of bubble growth, the volume fraction of exsolved volatiles, ascent rate, and most importantly to a critical elongation rate. The key point of this illustrative example is that the evolution to brittle failure occurs over a narrow depth interval, due to the nonlinear dependence of viscosity on crystal content and the feedback between viscosity, decompression rate and magma expansion. The system thus evolves invariably toward failure conditions, assuming that discharge rates are sufficiently high and magma crystallizes sufficiently fast.

4. Conclusion

Explosive and dangerous Plinian style eruptions of basaltic magma have been a subject of debate. Using a novel approach of combined oscillatory and extensional rheometry, we have investigated the viscoelastic properties of dense particulate suspensions that are dynamically similar to microcrystalline basaltic magma, as preserved in basaltic Plinian pyroclasts from Mt Etna, 122 BCE and Mt Tarawera, 1886. We find that such a suspension fractures brittly at elongation rates of about 1 s^{-1} or greater, while the particle-free suspending liquid does not fracture at such rates. We propose that basaltic magma with high volume fractions of crystals may also undergo brittle failure at such elongation rates, which are otherwise not sufficiently high to fracture crystal-free basalts. This study provides a basis for future investigations of viscoelastic rheology and extensional deformation of expanding multiphase magma during explosive volcanic eruptions. Using scaling analysis and numerical model of magma ascent in volcanic conduit, we show that high crystal volume fractions and critical elongation rate can potentially be reached during Plinian eruptions of crystallizing basaltic magma.

Notation

a	Fissure half width (m)
b	Fissure length (m)
B	Gas constant ($J\,mol^{-1}\,K^{-1}$)
c	Concentration of dissolved volatiles inside melt (wt%)
c_R	Concentration of volatiles at the vapor–melt interface (wt%)
Ca	Capillary number
d_0	Initial diameter of suspension filament under extension (m)
d_{mid}	Mid-diameter of suspension filament (m)
D_H	Diffusivity of H_2O ($m^2\,s^{-1}$)
$\dot{E}$	Axial stretch rate (s^{-1})
f_m	Friction factor
g	Gravitational acceleration ($m\,s^{-2}$)
F	Crystal growth rate ($m\,s^{-1}$)
G_∞	Infinite shear modulus (Pa)
G'	Storage modulus (Pa)
G''	Loss modulus (Pa)
G^*	Complex shear modulus (Pa)
h	Thickness of the sample in shear experiments (m)
I	Crystal nucleation rate ($m^{-3}\,s^{-1}$)
k	Boltzmann constant
k_v	Volumetric factor in Avrami equation
L_0	Initial gap between plates (m)
L_p	Position of upper moving plate (m)
$\dot{L}_p$	Speed of upper moving plate ($m\,s^{-1}$)
M	Mach number
M_w	Molecular weight of water ($kg\,mol^{-1}$)
n	Flow index
N_b	Bubble number density per unit volume of melt (m^{-3})
Oh	Ohnesorge number
p	Pressure of gas–pyroclast flow (Pa)
P_g	Gas pressure inside bubble (Pa)
P_m	Melt pressure outside bubble (Pa)
Pe	Peclet number
Q	Magma discharge rate ($kg\,s^{-1}$)
r_p	Particle radius (m)
R	Bubble radius (m)
Re	Reynolds number for magma ascent in conduit
Re_p	Particle Reynolds number
S	Half distance between two adjacent bubbles (m)
S_r	Radius of the sample-disk in shear experiments (m)
St	Stokes number
t	Time (s)
T	Magma temperature (°C)
T_K	Absolute temperature in Peclet number (°C)
u	Ascent rate ($m\,s^{-1}$)
u_f	Ascent rate at fragmentation ($m\,s^{-1}$)
u_p	Velocity of gas-pyroclast flow ($m\,s^{-1}$)
V_{mo}	Initial melt volume surrounding bubble (m^3)
V_m	Melt volume surrounding bubble (m^3)
V_x	Crystal volume in melt surrounding bubble (m^3)
z	Depth (m)
γ_{eff}	Effective extensional strain in tensile experiments
$\dot{\gamma}_{\text{eff}}$	Effective extensional strain rate (s^{-1}) in tensile experiments
$\dot{\gamma}_{\text{cr}}$	Critical rate of deformation for fragmentation (s^{-1})
γ_s	Shear strain
$\dot{\gamma}_s$	Shear rate (s^{-1})
$\dot{\gamma}_E$	Extensional rate (s^{-1}) in melt+crystal matrix surrounding growing bubble
σ	Surface tension ($N\,m^{-1}$)
ϕ	Volume fraction of vesicles or gas
ϕ_f	Gas volume fraction at fragmentation
ϕ_m	Maximum packing fraction of crystals
ϕ_{mb}	Maximum packing fraction of bubbles
ϕ_p	Gas volume fraction in gas-pyroclast flow
ϕ_x	Volume fraction of crystals in the groundmass
η	Viscosity of magma (Pa s)
η_m	Viscosity of basalt melt (Pa s)
η_l	Viscosity of suspending liquid (Pa s)
η_r	Ratio of melt+crystal+bubble viscosity to melt+crystal viscosity
η_x	Viscosity of melt+crystal matrix (Pa s)
ρ	Density of magma ($kg\,m^{-3}$)
ρ_g	Density of gas ($kg\,m^{-3}$)
ρ_l	Density of suspending liquid ($kg\,m^{-3}$)
ρ_m	Density of basalt melt ($kg\,m^{-3}$)
τ_{relax}	Relaxation time scale (s)

Acknowledgements

We thank T. Mather for editorial handling of the manuscript, as well as L. Wilson and an anonymous reviewer for their thoughtful comments. This research was not supported by any specific grant from funding agencies in the public, commercial, or not-for-profit sectors.

Appendix A. Dynamic similarity

To assess the dynamic similarity between our experimental conditions and the conditions during volcanic eruptions of crystalline basaltic magma, we define the rheophysical properties of the particulate suspension under shear using the dimensionless

Peclet number, Pe, Stokes number, St, and particle Reynolds number, Re_p, defined as (Stickel and Powell, 2005, and references therein)

$$\mathrm{Pe} = \frac{6\pi\eta_l r_p^3\dot{\gamma}}{kT_K},\quad \mathrm{Re}_p = \frac{\rho_l r_p^2\dot{\gamma}}{\eta_l},\quad \mathrm{St} = \frac{\rho_p r_p^2\dot{\gamma}}{\eta_l}. \tag{A.1}$$

Here k ($= 1.38\times10^{-23}$ JK^{-1}) is the Boltzmann constant, a is the suspended particle radius, T_K is the absolute temperature, η_l is the suspending liquid viscosity, ρ_l is the density of the suspending liquid, and ρ_p is the particle density. Pe is the ratio between hydrodynamic forces and forces of Brownian motion, Re_p is the ratio between inertial and viscous forces, and St is the ratio between the characteristic time scales of particle motion and shear deformation of the suspension. For the oscillatory shear experiments, the shear rate can be calculated as $\omega\gamma_s$ (Mezger, 2006), where ω is the angular frequency and γ_s is the shear strain or strain amplitude (Fig. 3). Thus for a range of shear rates ($10^{-4}-10^{1}$ s^{-1}), with particle density of 2500 kg m^{-3}, liquid density of ≈1000 kg m^{-3}, average particle radius of ≈ 6 μm and liquid viscosity of 100 Pa s, we find that Pe ≫ 1, St ≪ 1 and Re_p ≪ 1. This indicates that the experimental conditions were non-Brownian, with a strong liquid-particle coupling, whereas the inertial forces were negligible. For basaltic magma with 10–100 μm microlites, erupting at ascent velocities of about 1 m s^{-1} in a volcanic conduit of about 10–100 m in radius, or in an idealized dike of 1–10 m width, an order of magnitude estimate of shear rates is 10^{-3}–10^{0} s^{-1}. This corresponds to Pe ≫ 1, St ≪ 1 and Re_p ≪ 1, which are similar to the experimental conditions.

For deformation under extension the ratio of the viscous to capillary and inertial forces is defined by the Ohnesorge number, Oh, as (Villermaux, 2012)

$$\mathrm{Oh} = \frac{\eta}{\sqrt{\rho_l d_0\sigma}}, \tag{A.2}$$

where η is the viscosity of particulate suspension, d_0 is the initial diameter of the suspension filament, and σ is the surface tension. For an initial diameter of $d_0 \approx 0.005$ m for the filament in the elongation experiments, a suspension viscosity of $\sim 10^4 - 10^5$ Pa s, density of $\approx 10^3$ kg m^{-3}, and surface tension of $\approx 10^{-2}$ N m^{-1}, we estimate that Oh ≫ 1. This suggests that the capillary and inertial forces were negligible in the experiments. This is similar to magmatic conditions where Oh is also ≫ 1, assuming a melt and crystal bearing bubble wall thickness of about 1–10 μm, surface tension of about 10^{-1} N m^{-1}, and viscosity of about 10^5 to 10^6 Pa s.

Micro-crystals in basaltic Plinian pyroclasts (e.g., Fig. 1) are often bi- or poly-modal in size and shape, as opposed to the spherical particles in our analog experiments. This effects the relationship between ϕ_x and viscosity. It can, however, be accounted for by normalizing ϕ_x relative to the maximum packing fraction ϕ_m. The maximum packing fraction, ϕ_m, may be 0.6 or greater (Moitra and Gonnermann, 2015) for a distribution of large, high aspect ratio crystals and very small high aspect ratio or equigranular crystals, as can be observed in Fig. 1. Therefore, the microlite content of $0.6 \le \phi_x \le 0.9$ in the basaltic Plinian pyroclasts from Mt. Etna 122 BCE and Mt. Tarawera 1886 (Sable et al., 2006, 2009) are likely near the maximum packing. To this end, our experiments were conducted using a suspension with ϕ_x (0.55) close to ϕ_m (0.56).

Appendix B. Modeling of eruptive magma ascent

The model represents the ascent of crystallizing basaltic magma during eruptions and includes growth of bubbles, assumed to be monodisperse, spherical and homogeneously distributed (e.g., Proussevitch and Sahagian, 1998). The model is assumed time-invariant, because the eruption duration was longer than the magma ascent time scale (Slezin, 2003). Because exposures of basaltic Plinian eruption vent, such as at Tarawera, typically indicate a few-meter wide and partially back-filled feeder dike (Sable et al., 2009), we assume magma ascent within an idealized dike. Volatile exsolution and bubble growth cause a small degree of cooling (Proussevitch and Sahagian, 1998). This is approximately offset by the latent heat of crystallization (Mastin and Ghiorso, 2001), and therefore isothermal conditions are assumed. The model comprises the following set of equations:

$$\frac{d(\rho u)}{dz} = 0 \tag{B.1}$$

$$\frac{dP_m}{dz} = \left(-\rho g - \rho u^2\frac{f_m}{4a}\right)\left(1-M^2\right)^{-1} \tag{B.2}$$

$$\frac{dR}{dz} = \frac{R}{4\eta_x u}\left(P_g - P_m - \frac{2\sigma}{R}\right) \tag{B.3}$$

$$\frac{dc}{dz} = -\frac{4\pi R D_H(c-c_R)}{uV_m} + c\frac{d\phi_x}{dz}\frac{V_{mo}}{V_m} \tag{B.4}$$

$$\frac{dP_g}{dz} = \frac{3BT\rho_m D_H(c-c_R)}{R^2 M_w u} - \frac{3P_g}{R}\frac{dR}{dz} \tag{B.5}$$

$$\frac{d\phi_x}{dz} = (1/u)4k_v I F^3 t^3 \exp\left(-k_v I F^3 t^4\right) \tag{B.6}$$

$$\eta_x = \eta_m\left(1-\frac{\phi_x}{\phi_m}\right)^{-2}\dot{\gamma}_s^{n-1} \tag{B.7}$$

$$\eta_r\left[\frac{1-\frac{12}{5}\eta_r^2\mathrm{Ca}^2}{1-\frac{12}{5}\mathrm{Ca}^2}\right]^{-4/5} = \left[1-\frac{\phi}{\phi_{mb}}\right]^{-\phi_{mb}} \tag{B.8}$$

$$\eta = \eta_m\eta_r\left(1-\frac{\phi_x}{\phi_m}\right)^{-2}\dot{\gamma}_s^{n-1} \tag{B.9}$$

$$\rho_g\phi_f u_f = \rho_{gp}\phi_p u_p \tag{B.10}$$

$$(1-\phi_f)u_f = (1-\phi_p)u_p \tag{B.11}$$

$$p_m(1-\phi_f) + p_g\phi_f + \rho_m(1-\phi_f)u_f^2 + \rho_g\phi_f u_f^2 = p + \rho_m(1-\phi_p)u_p^2 + \rho_{gp}\phi_p u_p^2. \tag{B.12}$$

Equation (B.1) is the mass balance for magma in the dike. Equations (B.2) and (B.3) are the momentum balance equations for magma flow in the dike and for bubble inside the magma, respectively. Equation (B.4) represents the diffusion of volatiles inside bubbles, where the second term on the right hand side represents the rate of change in dissolved H_2O concentration due to microlite formation and subsequent reduction in melt volume, $V_{mo} - V_x$, where V_x ($= V_{mo}\phi_x$) is the total volume of crystals, and ϕ_x is the volume fraction of crystals. The diffusion of H_2O into the bubble is calculated using the mean field approximation (e.g., Toramaru, 1995). Equation (B.5) represents the change in gas pressure inside bubbles (Proussevitch et al., 1993). Equation (B.6) is the Avrami equation (Cashman, 1993) and represents the rate of change in crystal volume fraction of the melt. The shear-rate dependent change in magma viscosity, due to the presence of crystals and bubbles, is included through Equation (B.7) (Moitra and Gonnermann, 2015) and Equation (B.8) (Pal, 2003), respectively. η_x is the melt+crystal viscosity, and η_r is the ratio of melt+bubble+crystal viscosity to η_x. Thus, the bubble and crystal bearing magma viscosity, η in Equation (B.9), is based on the "effective medium" approach (e.g. Truby et al., 2015). For the post-fragmentation gas-pyroclast flow, mass balance of the gas phase and suspended pyroclasts are solved using equations (B.10) and (B.11), respectively. Equation (B.12) represents the momentum balance of the gas-pyroclast flow as a whole with a modified friction factor (e.g., Melnik et al., 2005; Koyaguchi et al., 2010). The viscosity of the

gas-pyroclast flow varies as a function of gas and pyroclast volume fractions (Mastin and Ghiorso, 2000).

In the above equations $u = Q/(\rho 2ab)$ is the magma ascent velocity, where $2ab$ is the cross-sectional area of the dike. Furthermore, $\rho = \rho_m(1-\phi) + \rho_g\phi$ is the density of magma with $\phi = R^3/S^3$ the gas volume fraction calculated from the bubble radius, R, and the half distance between two adjacent bubbles, S. f_m $(= 24/Re + 0.01)$ is the friction factor for the idealized dike (Wilson and Head, 1981) and $\mathrm{Re} = \rho u 2a/\eta$ is the Reynolds number. The rate of shear, $\dot{\gamma}_s$, used to calculate the shear-rate dependent viscosity of multiphase magma is defined as u/a in the model, where u is the magma ascent rate and a is the dike half width. M is the Mach number (e.g., Melnik et al., 2005). The solubility of H_2O is calculated as function of pressure, temperature and melt composition (Dixon, 1997). D_H is the diffusivity of H_2O (Zhang et al., 2007). $V_{mo} = 1/N_b$ is the initial melt volume surrounding one bubble and N_b is the bubble number density per unit volume of melt. The gas density, ρ_g, is calculated as a function of P_g using a modified Redlich–Kwong equation of state (Kerrick and Jacobs, 1981). The complete description of symbols is provided under 'Notation'.

Initial conditions for Fig. 6 are dissolved H_2O content of 3 wt% (Gamble et al., 1990), corresponding H_2O saturation pressure (Dixon, 1997), initial bubble radius of 10^{-6} μm, and zero initial volume fraction of crystals. We assumed a straight-sided dike with the exit condition at the surface as choked, defined by Mach number of M = 1 (Woods and Koyaguchi, 1994). It was matched by varying the magma discharge rate, Q. The system of Equations (B.1)–(B.6) was coupled and solved using MATLAB® solver `ode15s` (Shampine and Reichelt, 1997).

References

Applegarth, L., Tuffen, H., James, M., Pinkerton, H., 2013. Degassing-driven crystallisation in basalts. Earth-Sci. Rev. 116, 1–16.

Arzilli, F., Agostini, C., Landi, P., Fortunati, A., Mancini, L., Carroll, M., 2015. Plagioclase nucleation and growth kinetics in a hydrous basaltic melt by decompression experiments. Contrib. Mineral. Petrol. 170 (5–6), 55.

Bird, R., Stewart, W., Lightfoot, E., 2002. Transport Phenomena, second edition. John Wiley & Sons, Inc.

Brugger, C.R., Hammer, J.E., 2010. Crystallization kinetics in continuous decompression experiments: implications for interpreting natural magma ascent processes. J. Petrol. 51 (9), 1941–1965.

Campagnola, S., Romano, C., Mastin, L., Vona, A., 2016. Confort 15 model of conduit dynamics: applications to Pantelleria Green Tuff and Etna 122 BC eruptions. Contrib. Mineral. Petrol. 171 (6), 1–25.

Cashman, K.V., 1993. Relationship between plagioclase crystallization and cooling rate in basaltic melts. Contrib. Mineral. Petrol. 113 (1), 126–142.

Coltelli, M., Carlo, P.D., Vezzoli, L., 1998. Discovery of a Plinian basaltic eruption of Roman age at Etna volcano, Italy. Geology 26 (12), 1095–1098.

Costantini, L., Houghton, B.F., Bonadonna, C., 2010. Constraints on eruption dynamics of basaltic explosive activity derived from chemical and microtextural study: the example of the Fontana Lapilli Plinian eruption, Nicaragua. J. Volcanol. Geotherm. Res. 189 (3–4), 207–224.

Dingwell, D.B., Webb, S.L., 1989. Structural relaxation in silicate melts and non-newtonian melt rheology in geologic processes. Phys. Chem. Miner. 16 (5), 508–516.

Dixon, J.E., 1997. Degassing of alkalic basalts. Am. Mineral. 82 (3–4), 368–378.

Gamble, J.A., Smith, I.E., Graham, I.J., Kokelaar, B.P., Cole, J.W., Houghton, B.F., Wilson, C.J., 1990. The petrology, phase relations and tectonic setting of basalts from the Taupo Volcanic Zone, New Zealand and the Kermadec Island Arc–Havre Trough, SW Pacific. J. Volcanol. Geotherm. Res. 43, 253–270.

Giordano, D., Dingwell, D., 2003. Viscosity of hydrous Etna basalt: implications for Plinian-style basaltic eruptions. Bull. Volcanol. 65, 8–14.

Goepfert, K., Gardner, J.E., 2010. Influence of pre-eruptive storage conditions and volatile contents on explosive Plinian style eruptions of basic magma. Bull. Volcanol. 72 (5), 511–521.

Gonnermann, H.M., 2015. Magma fragmentation. Annu. Rev. Earth Planet. Sci. 43, 431–458.

Hammer, J.E., Rutherford, M.J., 2002. An experimental study of the kinetics of decompression-induced crystallization in silicic melt. J. Geophys. Res., Solid Earth 107 (B1).

Heymann, L., Peukert, S., Aksel, N., 2002. Investigation of the solid–liquid transition of highly concentrated suspensions in oscillatory amplitude sweeps. J. Rheol. 46 (1), 93–112.

Houghton, B.F., Gonnermann, H.M., 2008. Basaltic explosive volcanism: constraints from deposits and models. Chem. Erde, Geochem. 68 (2), 117–140.

Hui, H., Zhang, Y., 2007. Toward a general viscosity equation for natural anhydrous and hydrous silicate melts. Geochim. Cosmochim. Acta 71 (2), 403–416.

Kerrick, D., Jacobs, G., 1981. A modified Redlich–Kwong equation for H_2O, CO_2, and H_2O–CO_2 mixtures at elevated pressures and temperatures. Am. J. Sci. 281, 735–767.

Koyaguchi, T., Suzuki, Y.J., Kozono, T., 2010. Effects of the crater on eruption column dynamics. J. Geophys. Res., Solid Earth 115 (B7).

Mader, H.M., Llewellin, E.W., Mueller, S.P., 2013. The rheology of two-phase magmas: a review and analysis. J. Volcanol. Geotherm. Res. 257, 135–158.

Mastin, L.G., Ghiorso, M.S., 2000. A Numerical Program for Steady-State Flow of Magma–Gas Mixtures Through Vertical Eruptive Conduits. USGS Open-File Report 00-209, pp. 1–61.

Mastin, L.G., Ghiorso, M.S., 2001. Adiabatic temperature changes of magma–gas mixtures during ascent and eruption. Contrib. Mineral. Petrol. 141 (3), 307–321.

McKinley, G.H., Sridhar, T., 2002. Filament-stretching rheometry of complex fluids. Annu. Rev. Fluid Mech. 34 (1), 375–415.

Melnik, O., Barmin, A.A., Sparks, R.S.J., 2005. Dynamics of magma flow inside volcanic conduits with bubble overpressure buildup and gas loss through permeable magma. J. Volcanol. Geotherm. Res. 143 (1–3), 53–68.

Mezger, T.G., 2006. The Rheology Handbook: For Users of Rotational and Oscillatory Rheometers. Vincentz Network GmbH & Co KG.

Moitra, P., Gonnermann, H., 2015. Effects of crystal shape-and size-modality on magma rheology. Geochem. Geophys. Geosyst., 1–26.

Moitra, P., Gonnermann, H.M., Houghton, B.F., Giachetti, T., 2013. Relating vesicle shapes in pyroclasts to eruption styles. Bull. Volcanol. 75 (2), 1–14.

Namiki, A., Manga, M., 2008. Transition between fragmentation and permeable outgassing of low viscosity magmas. J. Volcanol. Geotherm. Res. 169 (1–2), 48–60.

Namiki, A., Tanaka, Y., 2017. Oscillatory rheology measurements of particle- and bubble-bearing fluids: solid-like behavior of a crystal-rich basaltic magma. Geophys. Res. Lett. 44 (17), 8804–8813.

Pal, R., 2003. Rheological behavior of bubble-bearing magmas. Earth Planet. Sci. Lett. 207 (1–4), 165–179.

Papale, P., 1999. Strain-induced magma fragmentation in explosive eruptions. Nature 397 (6718), 425–428.

Parfitt, E.A., 2004. A discussion of the mechanisms of explosive basaltic eruptions. J. Volcanol. Geotherm. Res. 134 (1), 77–107.

Proussevitch, A.A., Sahagian, D.L., 1998. Dynamics and energetics of bubble growth in magmas: analytical formulation and numerical modeling. J. Geophys. Res., Solid Earth 103 (B8), 18223–18251.

Proussevitch, A.A., Sahagian, D.L., Anderson, A.T., 1993. Dynamics of diffusive bubble growth in magmas: isothermal case. J. Geophys. Res. 98 (B12), 22283.

Sable, J.E., Houghton, B.F., Del Carlo, P., Coltelli, M., 2006. Changing conditions of magma ascent and fragmentation during the Etna 122 BC basaltic Plinian eruption: evidence from clast microtextures. J. Volcanol. Geotherm. Res. 158 (3–4), 333–354.

Sable, J.E., Houghton, B.F., Wilson, C.J.N., Carey, R.J., 2009. Eruption mechanisms during the climax of the Tarawera 1886 basaltic Plinian eruption inferred from microtextural characteristics-of the deposits. In: Special Publications of International Association of Volcanology and Chemistry of the Earth's Interior, pp. 129–154.

Shampine, L.F., Reichelt, M.W., 1997. The MATLAB ODE suite. SIAM J. Sci. Comput. 18 (1), 1–22.

Shea, T., Hammer, J.E., 2013. Kinetics of cooling- and decompression-induced crystallization in hydrous mafic-intermediate magmas. J. Volcanol. Geotherm. Res. 260, 127–145.

Slezin, Y.B., 2003. The mechanism of volcanic eruptions (a steady state approach). J. Volcanol. Geotherm. Res. 122 (1–2), 7–50.

Stickel, J.J., Powell, R.L., 2005. Fluid mechanics and rheology of dense suspensions. Annu. Rev. Fluid Mech. 37, 129–149.

Sumita, I., Manga, M., 2008. Suspension rheology under oscillatory shear and its geophysical implications. Earth Planet. Sci. Lett. 269 (3), 468–477.

Toramaru, A., 1995. Numerical study of nucleation and growth of bubbles in viscous magmas. J. Geophys. Res., Solid Earth 100 (B2), 1913–1931.

Truby, J., Mueller, S., Llewellin, E., Mader, H., 2015. The rheology of three-phase suspensions at low bubble capillary number. Proc. R. Soc. Lond. A, Math. Phys. Eng. Sci. 471 (2173), 20140557.

Valentine, G., Gregg, T., 2008. Continental basaltic volcanoes—processes and problems. J. Volcanol. Geotherm. Res. 177 (4), 857–873.

Villermaux, E., 2012. The formation of filamentary structures from molten silicates: Pele's hair, angel hair, and blown clinker. C. R., Méc. 340 (8), 555–564.

White, E.E.B., Chellamuthu, M., Rothstein, J.P., 2010. Extensional rheology of a shear-thickening cornstarch and water suspension. Rheol. Acta 49 (2), 119–129.

Wilson, L., Head, W.J., 1981. Ascent and eruption of basaltic magma on the earth and moon. J. Geophys. Res. 86, 2971–3001.

Woods, A.W., Koyaguchi, T., 1994. Transitions between explosive and effusive eruptions of silicic magmas. Nature 370 (6491), 641–644.

Zhang, Y., Xu, Z., Zhu, M., Wang, H., 2007. Silicate melt properties and volcanic eruptions. Rev. Geophys. 45 (4), 1–27.